The Feedback Between Stress, Faulting, and Fluid Flow:

Lessons from the Coso Geothermal Field, CA, USA

Nicholas C. Davatzes[1] and Stephen H. Hickman[2]

[1] 1901 N. 13th Street, Beury Hall, Temple University, Philadelphia, PA, 19122, USA, Davatzes@temple.edu

[2] Earthquake Hazards Team, U.S. Geological Survey, 345 Middlefield Rd., MS977, Menlo Park, CA 92405

Keywords: Coso, fault rock, stress, permeability, friction.

ABSTRACT

Surface mapping, mineralogical and micro-structural observations on core, cuttings and outcrop samples and borehole image logs indicate that variations in fault zone hydrology result from: (1) recurrent fracture slip driven by the remote stress; (2) changing fault zone mineralogy resulting from chemical alteration and healing localized along fractures; and (3) fracture connectivity. Brittle fracture and frictional slip in low porosity crystalline rocks produce dilation owing to surface roughness along fracture walls, brecciation, and micro-cracking. However, active precipitation and alteration in the geothermal system implies rapid sealing of fractures. Precipitated calcite and silica retain the brittle dilatant behavior responsible for permeability generation as revealed by crack-seal textures and brecciated cements. Conversely, fault rocks enriched in phyllosilicates demonstrate ductile behavior that minimizes dilation accompanying slip thus mitigating permeability regeneration. Over time, a fault core enriched in phyllosilicates acts as a persistent barrier to cross-fault flow, consistent with the separation of regions of distinct fluid inclusion chemistry and temperature gradient across major faults. In contrast, continued brittle fracture in the damage zone produces an episodically well-connected, vertically extensive, fracture network conducive to fault-parallel fluid flow consistent with localized temperature anomalies and mud losses in high density fracture networks adjacent to reservoir-scale faults. These variations in fault characteristics correlate with distinct zones of temperature gradient in the Navy's Coso Wash well 58A-10. Simple analytical solutions for 1-D heat transport and convective instability indicate that the long-term average permeability of shallow conductive regions dominated by phyllosilicate-rich fault zones must be $<10^{-17}$ m^2, whereas in convective deeper zones where brittle faulting dominates permeability $>10^{-13.0}$ m^2.

1. INTRODUCTION

In crystalline rock, faults and fractures provide the primary source of permeability. Yet the active precipitation of minerals and chemical alteration in many hydrothermal systems implies that fractures conducting fluids in the subsurface will often seal and permeability will be lost. In contrast, recurrent brittle fracture and frictional failure in low porosity crystalline rocks produce dilation owing to surface roughness along the fracture walls (Brown, 1987) and the formation of breccias and micro-cracks during fault slip (Lockner and Beeler, 2002). Faults and fractures sealed by the precipitation of common vein-filling minerals such as quartz or calcite retain this brittle (dilatant) behavior, as demonstrated by crack-seal textures in layered veins or the brecciation of fault cements. These minerals maintain the frictional strength of the fractures and enhance their cohesion. These processes lead to periodic permeability

enhancement associated with reactivation of optimally oriented and critically stressed fractures, which has been shown to be an important mechanism in maintaining high reservoir permeability in some geothermal systems (Hickman et al., 1998; Barton et al., 1998).

Alternatively, dissolution of crystalline rock by hydrothermal fluids reduces the strength of grain contacts and increases porosity in fracture walls (Boitnott, 2002). Chemical alteration can also produce increasing proportions of clays and other phyllosilicates, which promote ductile behavior and reduce frictional strength (Lockner and Beeler, 2002) while also reducing fault permeability (Crawford et al., 2002; Tembe et al., in press). The potential result of these processes is increased ductility of fault rocks that minimizes dilation accompanying slip and prevents regeneration of permeability.

Geothermal systems are commonly recognized to include a clay-rich caprock situated above a permeable reservoir zone, and at greater depth, a plastically deforming zone. In this contribution we explore how mineralogical and petrophysical properties associated with these zones in the Coso Geothermal Field (CGF) of Eastern California, USA control the mechanisms that accommodate deformation and consequently determine the permeability of newly formed or reactivated fractures. We find that the permeability structure of the CGF is likely generated and maintained through a feedback between recurrent fracture slip and fluid flow on one hand and mineral precipitation and chemical alteration on the other. This manuscript summarizes a series of studies investigating the physical properties of fractures and faults hosting fluid flow in the CGF, the modern stresses that cause fracture formation and slip, and the resulting distribution of permeability in the geothermal system.

2. GEOLOGIC SETTING AND THE FAULT NETWORK

The CGF is located along the western edge of the Eastern California Shear Zone (Figure 1), subjected to both strike-slip and normal faulting. The field is situated in diorite, quartz diorite, granodiorite, and minor basalt above a partially molten magma body at depths as shallow as 4-5 km (Wicks et al., 2001; Monastero et al., 2005; Unruh and Hauksson, 2003; Manley and Bacon, 2001). These depths correspond to a cut-off in seismicity that is presumed to represent the brittle-ductile transition (Figure 1b inset) (Monastero et al., 2005). At the surface, intrusion of the magma body has resulted in Pliocene to recent rhyolite domes and basalt flows (Duffield et al., 1980) (Figure 1a). Unruh et al. (2002) and Monastero et al (2005) suggest that Coso lies within the right (releasing) step between the right lateral Little Lake fault zone to the SW and the Wild Horse Mesa fault to the NE, which are associated with strike-slip focal mechanisms. This zone accommodates 6.5±0.7
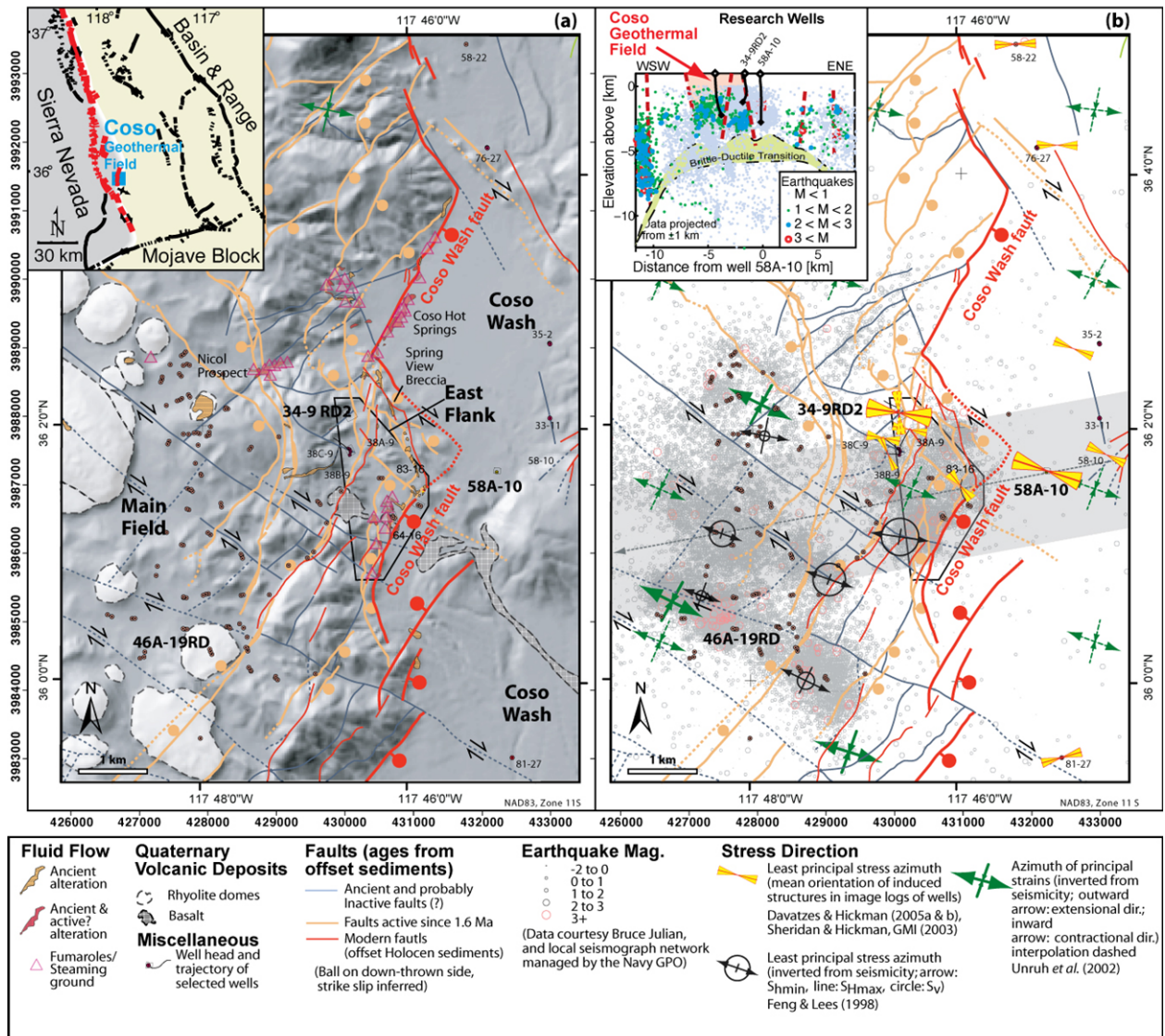
Figure 1: (a) Tectonic map of the east flank of the Coso Geothermal Field (CGF) over shaded relief image of topography. Location of alteration, fumaroles, and steaming ground is based on new mapping and results from Hulen (1978), Duffield et al. (1980), Whitmarsh (1998), Jayko (Personal communication, 2004), and work by Unruh and Streig (2004), and Unruh and Hauksson (2006). Inset in upper left shows the location of the field in the Owen's Valley east of the Sierra Nevada Mountains of California (Modified from Unruh, 2003). (b) Minimum horizontal stress orientations inferred from borehole image logs from Geomechanics International (2003), Sheridan et al. (2003), Sheridan and Hickman (2004) and Davatzes and Hickman (2005a). Wells discussed in this paper are indicated, as are stresses and incremental strains inferred from clusters of seismicity from 1980 to 1995 (Feng and Lees, 1998) and 1980 to 1998 (Unruh et al., 2002). Both analyses combine data from the Southern California Seismic Network with the local seismic array at Coso maintained by the Navy Geothermal Program office (GPO). Inset in (b), cross section of seismicity from 1993 to 2003 at the CGF recorded by the local seismometer network operated by the GPO. We infer that the brittle-ductile transition roughly coincides with the abrupt decrease in earthquake occurrence with increasing depth. Also shown are locations of well 34-9RD2, well 46A-19RD, and well 58A-10, the latter in Coso Wash outside the geothermal reservoir.

mm/year dextral shearing (McCluskey et al., 2001; Monastero et al., 2005).

Faults within the CGF can be broken into two distinct groups based on their geometry and inferred style of faulting. One group consists of WNW trending and minor NE trending faults that are interpreted as dextral and sinistral strike-slip faults, respectively, by Duffield et al. (1980) and Roquemore (1984) (Figure 1a). Many of these faults extend well outside the field and form prominent lineaments. They are exposed most often in bedrock and do not clearly offset any Quaternary sediment, but are associated with diffuse micro-seismicity in the geothermal field and with some

minor geomorphic expression. The relationship of the diffuse cloud of seismicity to the faults is difficult to interpret at this time, and we interpret these faults to be relatively inactive.

The other group consists of normal faults that dominantly trend N to NNE and dip both west and east (Figure 1a). The most prominent of these fault systems is the Coso Wash normal fault, which coincides with the eastern margin of the geothermal field. It is composed of several en-echelon NNE-SSW trending segments variably connected by NW-trending, probably oblique-slip faults. Normal faults appear to have been active in the Quaternary based on geomorphic

2

expression (Angela Jayko, pers. comm. 2004), offset hydrothermal deposits (Hulen, 1978), and offset basalt flows (Figure 1a). A subset of this normal fault population also offsets Holocene basin sediments (Unruh and Streig, 2004), creates local sediment catchments and fault scarps and is associated with seismicity (Figure 1b). Thus, we interpret these faults to be actively slipping.

The normal faults divide the geothermal field into three main geologic sub-regions: 1) the Main Field, 2) a central spine of exposed bedrock, which includes the East Flank region, and 3) Coso Wash. The Main Field is associated with high seismicity rates, high temperatures (>640ºF at <10,000 ft depth), and Quaternary rhyolite domes (Bishop and Bird, 1987). The spine of exposed bedrock extends north to south, and its intensely normal faulted eastern margin hosts the East Flank reservoir. With the exception of the East Flank region, which is associated with high temperatures and seismicity, the central region is largely aseismic and cool (Lutz *et al.*, 1996). The East Flank also stands out from the rest of this area because of the high normal fault density roughly located on the footwall side of a step between two Coso Wash normal fault segments. Coso Wash is a series of sub-basins associated with segments of the Coso Wash fault and experiences the least seismicity and lowest temperatures (Davatzes and Hickman, 2005b). The intersection of the N to NNE normal faults with the WNW faults dissects all three regions of the geothermal field into rhombohedral fault-bounded volumes.

3 FRACTURE & FAULT ZONE CHARACTERISTICS

Previous studies have revealed that the minerals that comprise fault rock, their grain shapes, and packing geometry are important controls on fault zone properties such as permeability (Crawford et al., 2002), and frictional strength and slip behavior (Lockner and Beeler, 2002; Tembe et al., in press). The textural and mineralogical evolution of fault rocks with increasing shear strain is revealed by detailed analysis of core from well 64-16 and surface examples of exhumed fault zones (Davatzes and Hickman, 2005). We used outcrop and hand-sample scale mapping, X-Ray Diffraction (XRD) analysis, and Scanning Electron Microscopy (SEM) secondary electron images of fault gouge and slip surfaces at different stages of development (estimated shear strain) to investigate the processes responsible for the development and physical properties of these distinct fault rocks.

Our examination of the mineralogy and microstructure of fault rock at Coso reveals three fault rock types (Davatzes and Hickman, 2005b): (1) Fault rock consisting of poorly sorted dilatant breccia, characterized by large variations in grain packing (pore size) and calcite crack-seal textures. (2) Fault rock consisting of amorphous silica and zeolites that contains large connected pores, dilatant brittle fractures, and dissolution textures. (3) Fault rock consisting of foliated layers of chlorite and illite-smectite separated by slip surfaces. These different fault rocks are respectively associated with a high permeability convectively heated reservoir zone in the geothermal system, a shallow region of boiling promoting acid alteration and dissolution of the rock mass, and a conductively heated "caprock" at moderate to shallow depth associated with low permeability.

3.1 Brecciated, Dilatant, Calcite or Silica/Quartz-Rich Fault Zone

Fault zone development associated with repeated episodes of brittle failure, shearing, and healing for this type of fault

zone is illustrated in Figure 2. Damage of the intact crystalline rocks is first comprised of a series of small faults and fractures (Figure 2, t_0). As in the outcrop case, dilatant (tensile) fractures that abut the sheared fracture are anti-symmetrically distributed about sheared fractures at angles approximately between 50º and 75º (Figure 2, t_1) where they define fracture-bounded rhombs of rock and localize dilatancy. This geometry and age relationship is consistent with the formation of splay fractures that propagate in response to tensile stresses concentrated at the tip or at asperities of a slipping shear fracture (Davatzes and Aydin, 2003). Splay fractures are densest in extensional steps between two overlapping, *en echelon* sheared fractures. Reactivation of fractures healed by precipitation (Figure 2, t_2) is associated with the rotation of the fracture-bounded volumes and the formation of breccia, indicating that fracture porosity is regenerated following healing. Development of multiple sets of crosscutting cements in fault-hosted breccias indicates successive episodes of fault reactivation, brittle fracturing accompanied by dilatancy, and healing of the regenerated porosity (Figure 2, t_3).

This kind of fault architecture is also consistent with breccia and dilatant fractures that dominate the damage zone of the Coso Wash normal fault exposed NNE of the Coso Wash Hot Springs (Davatzes and Hickman, 2005b). At that location, the damage zone is comprised of a series of small faults and fractures that mirror the local orientation of the modern fault scarp in the basin sediments. Many of these fractures contain fibrous veins more than 10 cm thick consistent with deposition into void space associated with splay fractures resulting from shear on older fractures.

3.2 Pervasively Altered Fault Rocks Rich in Clays, Zeolites, and Silica due to Acid Alteration

An example of an acid-altered normal fault zone is exposed by excavation of the mercury mine at the Nicol Prospect (Figure 3). The fault zone consists of an intensely altered fault core (the part of the fault that accommodates most of the deformation and shear strain) surrounded by highly fractured rocks comprising a damage zone with minor mineralization and small slickensided faults exhibiting several centimeters of down-dip (normal faulting) slip (Figure 3a). The fault core is comprised of gouge rich in amorphous silica with associated chlorite, illite, and zeolites (Figure 3b) and isolated breccia clasts of altered host rock (Figure 3c and d) (Davatzes et al., 2006). Most major rock-forming minerals such as hornblende and biotite are absent in the fault gouge (XRD analysis in Davatzes et al., 2006), although these are common rock-forming minerals in the surrounding host rock. However, remnant potassium-feldspar and quartz persists in the fault rock. In the breccia clasts, these minerals appear to have been leached out, increasing the porosity, and were partly replaced with alteration phases and amorphous silica.

The gouge zone contains a through-going striated slip surface and subsidiary shorter slip surfaces (Figure 3a). The through-going slip surfaces are coated by and incorporate microspheres of amorphous silica, called lepispheres (Figure 3b). Below this coating, the gouge is composed of slightly foliated platy clays, chlorite, and zeolites. The localized coating of the through-going slip surfaces by lepispheres (Rodgers et al., 2004) indicates that the silica was precipitated while suspended in flowing water moving along the slip surfaces. Within the fault core and altered damage zone, some pore collapse is evident. This occurs in the core adjacent to the slip surface where there is an alignment of platy minerals producing a pervasive foliation. In the
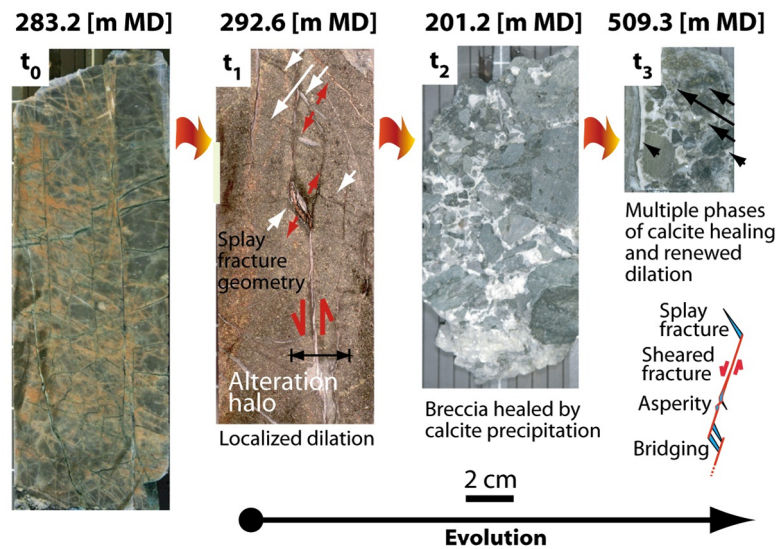
Figure 2: Core samples demonstrating the progression of deformation and healing in cataclastic fault rock within low porosity granitic rocks typical of the Coso Geothermal Reservoir. Samples are from Coso East Flank well 64-16, with shear strain increasing from left to right. Initial failure, t_0, includes macroscopic fracturing, brecciation and dilation followed by healing by mineral precipitation and then renewed fracturing and dilation.
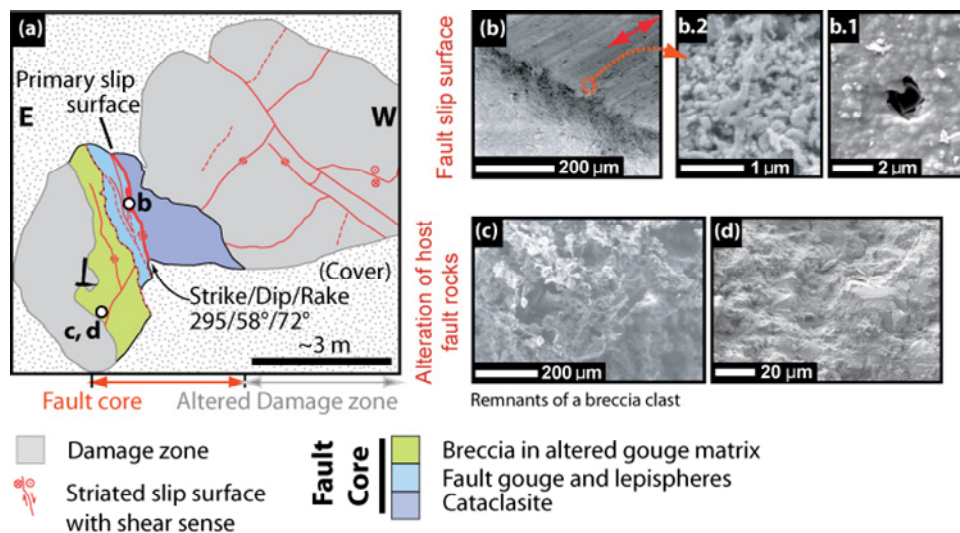

Figure 3: (a) Cross-sectional outcrop map of a normal fault zone undergoing acid alteration as part of active steaming ground and fumarole activity at the Nicol Prospect. The fault zone is characterized by distinct slip surfaces in a fault core that accommodates the majority of shear strain, with zones containing breccia and fractured and sheared rock forming a damage zone surrounding the fault core. Location of the Nicol Prospect is indicated in Figure 1. To the right are scanning Electron Microscope (SEM) secondary electron images of rock chips from the fault zone (locations in a). Upper series of images are from the primary slip surface of the fault zone. (b) Striated slip surface underlain by zeolite and clay-rich gouge with minor foliation development. (b.2), details of the slip surface show the coating of lepispheres that merge together over time (b.1) as amorphous silica locally dissolves and re-precipitates. In b.2, long tube-like structures are bacteria that live in the upwelling fluids in the fault zone and help mediate silica precipitation. Along the bottom row are materials from the breccia zone. (c) Most primary minerals have been leached away leaving a hollow framework of clays and zeolites. (d) In the regional adjacent to the fault core, a concoidally fractured quartz grain is the sole remaining primary mineral, illustrating another mechanism of quartz enrichment in fault zones.

damage zone where chemical alteration has changed rock into a loose aggregate of grains, there appear to be deformation band-like structures (Antonellini and Aydin, 1995; Aydin, 1978).

Taken together, the distribution of alteration and the occurrence of lepispheres are consistent with fluid flow primarily focused along the slip surface and bleeding out into the surrounding gouge and fractured damage zone.

3.3 Chlorite-Smectite Rich Fault Zone

The third fault zone type is distinguished by a fault core dominantly composed of chlorite and illite-smectite. Early development of these fault zones is similar to the previous examples, involving dilatant failure of the crystalline host rock associated with splay fracture and potentially the development of breccias (Figure 2, $t_{0,1}$). However, subsequent to initial failure, fault rock development is

dominated by the progressive alteration of the host rock and the precipitation of clay minerals (Figure 4, t_1). Adjacent to the fault core, deformation in the country rock is associated with formation of dilatant fractures, which can be subsequently healed by calcite (Figure 4, t_2). These fractures have the geometry of the splay fractures interpreted in Figure 2, but are confined to the host rock and do not develop in the clay-rich fault rock. At higher shear strains we note breccia and brittle fractures in the damage zone that are well-connected and dense, but also do not extend across the fault core (Figure 4, t_3).
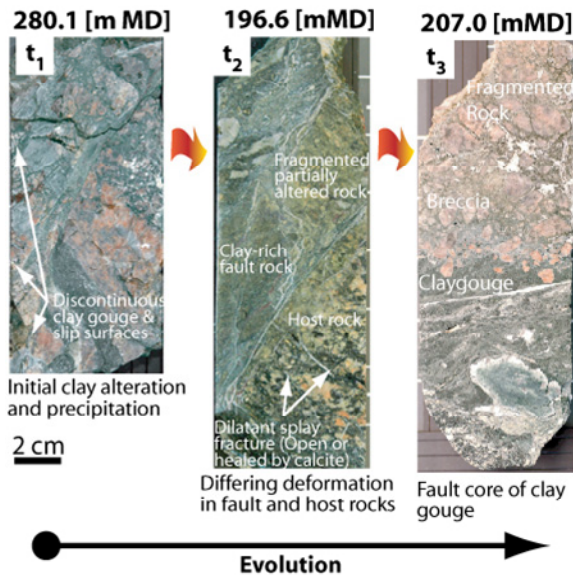

Figure 4: Core samples from Coso well 64-16 demonstrating the progression of deformation and alteration during development of clay-rich fault rock. Shear strain increases from left to right.

The fault core and associated slip surfaces in this type of fault is rich in chlorite and illite-smectite, defining a clay-rich fault core (see XRD analysis in Davatzes et al., 2006). Within the shear zone the chlorite shows foliation subparallel to the margins of the gouge. The textural relationship of the fault rock to the breccia blocks at the margins of the fault core indicates relatively ductile deformation by folding of foliated chlorite and smectite around breccia clasts and extrusion of clay into mesoscopic void space (Figure 4).

Multiple, linking slip surfaces are distributed across the fault core and anastomoze around more intact blocks of the host rock (Figure 4). Shear is localized in the clay-rich fault rock, while the boundaries of the fault core continue to undergo brittle failure and breccia development. These processes suggest that the fault zone can thicken by both continued alteration/precipitation of clays in the core and brittle deformation in the damage zone.

Detailed microstructural analysis of core from Coso well 64-16 reveals the processes by which these clay-rich fault zones evolve with shear strain (Figure 5). The gouge is composed of many polished and striated slip surfaces coated by illite-smectite separating very thin layers of chlorite- or illite-rich gouge. The SEM images (Figure 5b) illustrate a progressive development from poorly developed, short slip surfaces (t_1 and t_{1b}), to more extensive through-going boundary shears at higher shear strain (t_3). (1) At early stages (Figure 5b, image t_{1a}) the packages of gouge composed of generally equant illite and illite-smectite grains ranging in size from 0.05-2

microns, are also evident at this stage. Bending and irregular grain boundaries suggest some comminution has taken place. Distinct layers of this gouge are separated by poorly packed, striated slip surfaces. The edges of the gouge layers are associated with euhedral chlorite grains, with in-plane dimensions of ≤10 microns, growing into open pore space. (2) Continued shearing produces a poorly organized slip surface formed by the rotation, folding, and compaction, with minor comminution, of chlorite grains (Figure 5b, t_{1b}) between illite gouge layers. (3) This process produces a package of multiple layers of illite and chlorite gouge separated by slip surfaces (Figure 5b, t_2). Striations on the slip surfaces between these layers record a different direction of slip (green arrows) at a length-scale of about 20 μm. The variability in slip direction reflects the ability of the gouge to flow into void space as noted at location 1 in Figure 5a. (4) At even greater shear strains, the slip surfaces become more well-developed, consisting of aligned striated, tightly packed clay minerals acting as the primary shear surface in the fault zone mapped above (Figure 5b, t_3). This surface is preferentially associated with a coating of illite grains.
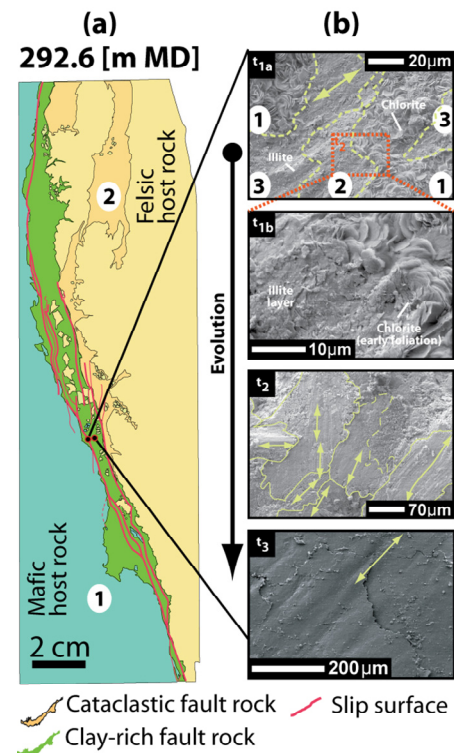

Figure 5: (a) Map of clay-rich fault zone from 990 ft MD in well 64-16 showing a well-developed fault core comprised of foliated chlorite, illite, and illite-smectite fault rocks. Site 1 in this map shows where clay-rich fault gouge has expanded and intruded into irregularities in the margins of the fault core. Site 2 illustrates cataclastic fault rock that predates the clay-rich core and was subsequently incorporated (tan fragments). (b) SEM secondary electron images and XRD of slip surfaces from the clay-rich fault zone revealing illite, illite-smectite, and chlorite laminations. Green arrows indicate slip direction, and dashed lines indicate boundaries between numbered microstructural domains (see text).

The pore geometry in clay-rich fault rock is largely bimodal. Large pores up to a few 10's of microns occur along the margins of gouge layers. However, the rotation and folding

of the chlorite grains in these locations produces flat, tortuous pore systems. In contrast, pore dimensions within the gouge layers are fairly uniform with diameters ≤0.1-0.01 micron. A third population, representing a minor fraction of the total porosity is located *in* the well-developed slip surfaces mapped in Figure 5a. Pores across these slip surfaces are limited to <10 nm.

4. STRESS

We used two main techniques to determine the magnitudes of the minimum horizontal principal stress, S_{hmin}, and the maximum horizontal principal stress, S_{Hmax}, in the East Flank. The magnitude of S_{hmin} was determined from hydraulic fracturing stress tests conducted in wells 38C-9 (Sheridan and Hickman, 2004) and 34-9RD2 (Davatzes and Hickman, 2006a). Upper bounds on the magnitudes of S_{Hmax} were obtained through borehole failure analyses and rock mechanics data on representative core from well 34-9RD2 (Morrow and Lockner, 2006) and from well 64-16 (TerraTek, 2004) and based upon the absence of breakouts in wells 34-9RD2 and 38C-9 in the East Flank and the presence (and width) of breakouts seen in well 58A-10 (Davatzes et al., 2006). In the subsequent text we limit our discussion to the implications of the stress model presented in Figure 6, without extensive explanation of the model derivation and direct the interested reader to the references cited above. This model is for pre-production conditions, to inform our evaluation of the development of structures that evolved in concert with the heating of the geothermal system. These models allow us to evaluate the propensity for shear failure on optimally oriented or individual existing faults as a potential control on fracture permeability.

In accordance with the Coulomb failure criterion, frictional failure (*i.e.*, normal faulting) would then occur at a critical magnitude of S_{hmin} given by (Jaeger and Cook, 1979):

$$S_{hmin\ crit} = (S_v - P_f) / [(\mu^2 + 1)^{1/2} + \mu]^2 + P_f \qquad (1)$$

Where S_V is the vertical principal stress, P_f is the formation fluid pressure and μ is the coefficient of friction of pre-existing faults. It is assumed here that μ ranges from 0.6 to 1.0, in accord with laboratory sliding experiments on a variety of rock types (Byerlee, 1978) and laboratory tests on core from Coso (TerraTek, 2004; Morrow and Lockner, 2006). These tests indicate that $\mu \sim$ 0.75 to 1.0 on fresh fracture surfaces of Coso core, with $\mu \sim$ 0.8 being most representative of diorite typical of the CGF. Similarly, this analysis can be repeated for frictional failure on optimally oriented strike-slip faults as:

$$S_{Hmax\ crit} = (S_{Hmin} - P_f) / [(\mu^2 + 1)^{1/2} + \mu]^2 + P_f \qquad (2)$$

Using Equation 4.1 we calculated the range of S_{hmin} magnitudes at which normal faulting would be expected along optimally oriented faults (Figure 6a). The measurements of S_{hmin} in wells 34-9RD2 and nearby well 38C-9 define the depth variation of S_{hmin} in the East Flank (Figure 6). Rearranging equation 4.1 to solve for μ, the measured or calculated values of P_f, S_V and S_{hmin} suggest that optimally oriented faults with $\mu > 0.44$ should be stable if normal faulting predominates in the East Flank. Similarly, using Equation 4.2 and extrapolating S_{hmin} measured in the East Flank to Coso Wash suggests that the S_{Hmax} magnitude from well 58A-10 (blue symbol in Figure 6) is close to the critical value for frictional failure on optimally oriented strike-slip faults for $\mu < 0.8$ to 1.0. As noted above, these values of μ are comparable to those measured on Coso core, suggesting that optimally oriented strike-slip faults in Coso Wash and

perhaps also the East Flank should be critically stressed for frictional failure (Figure 6a).

These stress boundary conditions also allow us to estimate the potential for shear failure on large-scale (mapped) faults of known orientation in the CGF (Figure 6b). This model uses the magnitude of S_{Hmax} from Coso Wash (Figure 6a, blue symbol) and applies it to the East Flank and Main Field with P_f appropriate for the higher temperature gradient in this region and S_V reflecting crystalline basement rocks to the surface. The magnitude of S_{Hmax} calculated for Coso Wash is compatible with the upper bounds required by the lack of breakouts in the East Flank (Figure 6a, open symbols). This model predicts active oblique slip on most of the mapped normal faults for μ ranging from ~0.4 to 0.8. As shown in Figure 6b, this lies between μ measured on fresh fracture surfaces in Coso cores (TerraTek, 2004; Morrow and Lockner, 2006) and μ expected for weak clay minerals in phyllosilicate-rich fault zones (Lockner and Beeler, 2002) This prediction is compatible with the mapped slip history (Figure 1a) and with earthquake occurrence throughout the CGF with a variety of normal-faulting and oblique-slip focal mechanisms (e.g., Feng and Lees, 1998; Unruh *et al.,* 2002; Monastero *et al.*, 2005). However, the stress model predicts that mapped NW-SE trending strike-slip faults within the CGF (c.f., Figure 1a and 6b) should not be active within the present-day stress field, which is consistent with the relative absence of recent activity indicated for these structures (discussed above).

Detailed examination of variations in borehole failure orientations with depth reveals numerous localized stress rotations in wells 34-9RD2 and 58A-10 (Davatzes and Hickman, 2006a; 2009). Our preliminary modeling of these local rotations in S_{hmin} (not presented here) suggests that they result from slip on faults, indicating active deformation in the East Flank and adjacent Coso Wash. These stress rotations generally occur adjacent to large-aperture faults visible in image logs (*e.g.*, Davatzes and Hickman, 2005a) at a variety of wavelengths and with amplitudes of up to 70º. These stress rotations suggest on-going fault slip at a variety of scales within and adjacent to the CGF.

5 FLUID FLOW

5. 1 Surface Manifestations of Fluid Flow Along Faults

Surface expressions of hydrothermal fluid flow in the CGF are steaming ground, fumaroles, and hydrothermal alteration/deposition, including acid alteration (Figures 1 and 3) (Hulen, 1978; Roquemore, 1981; Adams *et al*., 2000) (Figure 1a). These features are preferentially distributed along major NNE-SSW trending normal faults of Holocene to Quaternary age. Intersections between NNE-SSW trending faults and nearly WNW-ESE trending faults (Figure 1a) also appear to localize intense hydrothermal activity. These circumstances suggest that fluid flow is largely focused along the most recently active faults and fractures in the CGF, which is supported by the slip tendency of faults inferred from the modern stress state (Figure 6b). In addition, intense hydrothermal activity at some fault intersections suggests focusing of fluid flow where fault interactions promote dilatant failure that would increase and maintain permeability. However, simple analysis of the fault geometry and stress state does not entirely account for variations in the distribution of hydrothermal activity. Other variables such as the physical properties of fault rocks, reservoir engineering practices, and the complex 3D fault geometry and mechanical interactions between nearby faults under the current stress field are other possible factors, which will be addressed in a future study.
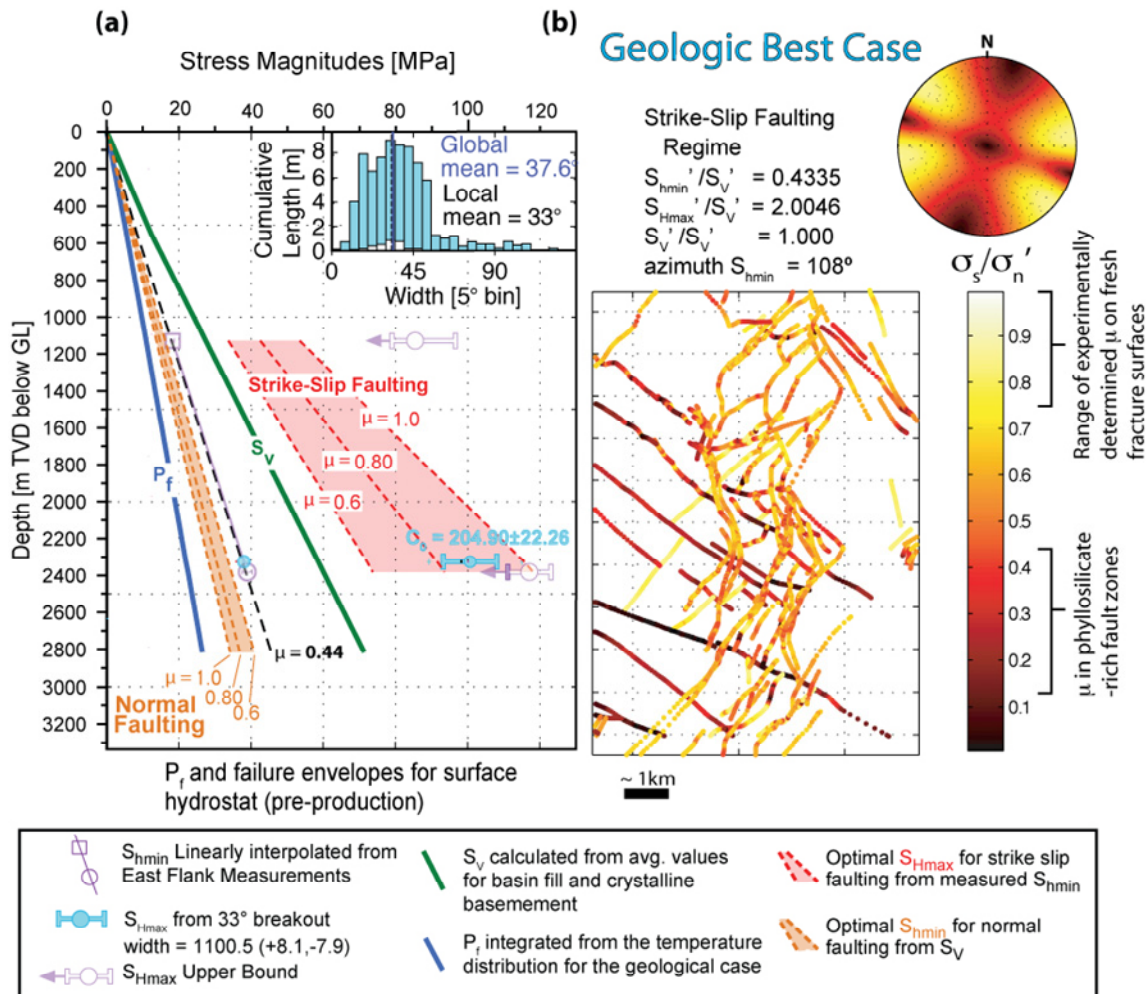
Figure 6: (a) Stress model for the East Flank and Coso Wash (Davatzes and Hickman, 2006a; Davatzes et al., 2006). (b) Map showing slip tendency of faults in the CGF based upon this stress model for the appropriate fault orientations (Davatzes and Hickman, 2006b).

5.2 Subsurface Hydrologic Behavior of Faults

Localized subsurface fluid flow along faults is indicated by short wavelength perturbations in borehole equilibrium and non-equilibrium temperature logs (see discussion in Barton et al., 1998) and mud losses that coincide with faults visible in image logs (analysis of well 58A-10 presented in Davatzes and Hickman, 2009). A detailed examination of faults and fractures in these distinct zones and the occurrence of localized temperature anomalies revealed a strong correlation between fault zone permeability and either the clay content of the fault zone or the slip tendency of the faults in the current stress field. In the subsurface we were able to interpret the distribution of clay/alteration mineralogy from cuttings (including new XRD observations and data from mud logs) and the textural attributes of fault zones visible in borehole televiewer (BHTV) and Formation MicroScanner (FMS) image logs (Figure 7). Our results indicate that clay-rich fault zones identified in cuttings are often associated with foliated textures in both types of image logs, enhanced micro-conductivity in FMS images (darker areas in Figure 7), and with anomalies in other wireline logs including increased caliper dimensions, reduced sonic velocity, anomalous neutron porosity, and increased natural gamma. These textures are similar to those we have examined visually in core from well 64-16 (section 3.3).

In general, individual fractures of all orientations and slip tendency occur at any depth range in well logs of the CGF (Sheridan et al., 2003; Sheridan and Hickman, 2004;

Davatzes et al., 2006; Davatzes and Hickman, 2006a, b, 2009). However, our analysis also shows that regions of higher temperature gradient are dominated by clay-rich fault rocks (e.g., faults at 2690 and 3861 ft MD in Figure 7). XRD analyses of these zones are associated either with spikes in clay content, or in the case of excessive washing of cuttings (typical of 58A-10), with a loss of mafic minerals, plagioclase, and feldspar, presumably depleted due to hydrothermal alteration. These clay-rich and hydrothermally depleted faults are essentially absent in zones of convective heat transfer where open fractures dominate (e.g., faults at 4712 ft MD and 7722 ft MD in Figure 7). In these convective regions, fault zones generally display cataclastic textures or clean fracture traces in borehole image logs (Figure 7), and are often associated with high fracture densities (Davatzes and Hickman, 2005a, 2009).

It is more difficult to determine where faults act as barriers to fluid flow, although this can be inferred from borehole temperature logs and the distribution of microseismicity. In well 58A-10 (Figure 8), very small but abrupt changes in geothermal gradient in the convective region of the reservoir (Zone 3) are associated with faults visible in image logs, which are also located at contacts between temperature gradient sub-zones. As the rocks in this interval are lithologically homogeneous (and presumably of uniform thermal conductivity), these small-scale transitions in gradient are consistent with these faults acting as limited barriers to fluid flow. In addition to vertical heterogeneity in permeability, strong later variations in permeability are
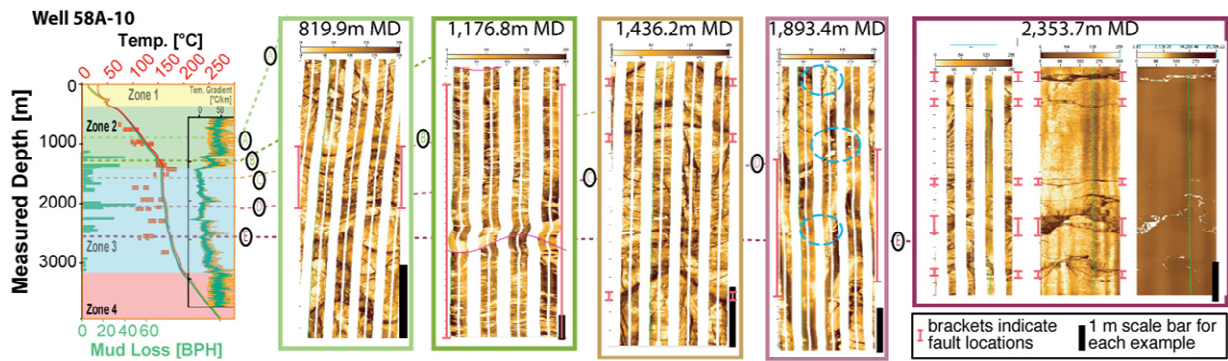
Figure 7: Examples of faults and fractures in regions of different geothermal gradient in well 58A-10, as seen in FMS (striped) and BHTV (solid) logs. The near-isothermal zone indicated by the temperature log (solid line) and fluid inclusion homogenization temperatures (dots) coincides with the greatest mud losses and fractures characterized by brittle textures Letters A-E in temperature profile correspond to fracture features indicated by red vertical bars, sinusoidal red line, and blue ovals in corresponding image logs.
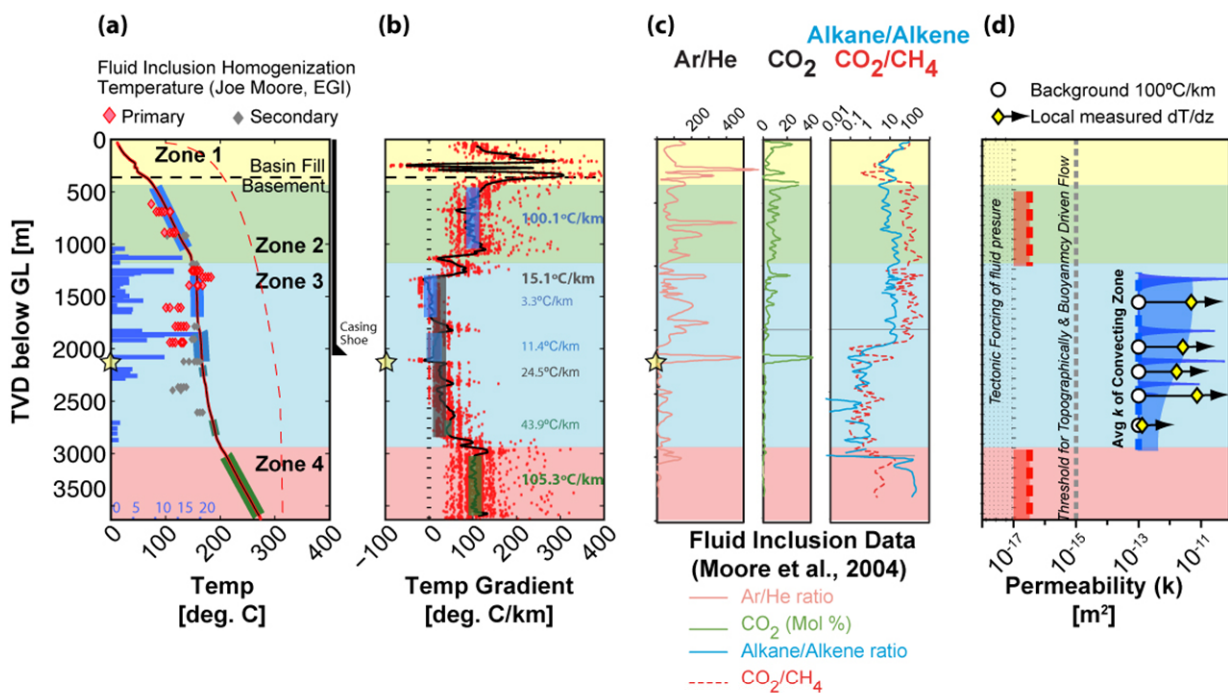

Figure 8: (a) Temperature profile of well 58A-10 in true vertical depth below the ground level. Red diamonds indicate primary and gray diamonds indicate secondary fluid inclusion temperatures. Horizontal blue bars indicate mud loss in barrels/hour (scale at bottom). Wide bars underlying the temperature profile indicate zones where we calculated average temperature gradients. Distinct zones of temperature gradient are designated Zone 1 through 4 and color-coded. (b) Temperature gradient, including discrete points, running average (solid line) and interval averages (bars with color-coded values). (c) Fluid inclusion gas chemistry (Moore et al., 2004). (d) Inferred permeability profile derived from average temperature gradients. Arrows indicate locations of local temperature anomalies associated with focused fluid flow and with faults visible in image logs. The permeability ranges required for tectonic forcing of fluid over-pressure and the threshold for buoyancy driven fluid flow are indicated (Ingebritsen and Sanford, 1998).

evident in the CGF. Two distinct compartments –the Main Field and East Flank– are bounded by faults visible at the surface (Figure 1b) and separated from each other and from neighboring compartments by zones of reduced permeability and lower temperature fluids (Mike Adams, pers. comm., 2003). This large-scale hydrologic compartmentalization is consistent with sharp margins to otherwise diffuse micro-seismicity within the actively produced CGF, which has been attributed to fluid pressure variations induced by changes in fluid production or injection (Feng and Lees, 1998). These sharply defined terminations of seismicity indicate that these faults act as barriers to fluid flow, limiting

the spatial extent of fluid pressure variation and effectively compartmentalizing the CGF.

In some locations, faults display indications of both focused fluid flow and barrier behavior. One example is the fault at 2103 m in well 58A-10 (Figure 8, indicated by yellow star), which was associated with significant mud losses while drilling and persistent negative temperature gradients, indicating relatively high permeability along the fault. This fault also separates adjacent sub-zones of distinct temperature gradient, suggesting that it may also function as a barrier to cross-fault fluid flow. Similarly, the Coso Wash

normal fault system (Figure 1a) hosts fumaroles but also defines the margins of on-going miroseismicity (Figure 1b). In both cases fluid flow across the fault appears to be inhibited, whereas fluid flow along the fault is enhanced.

5.3 Estimating Long-Term Permeability Variation

Variations in temperature gradient measured in wells such as 58A-10 can be used to estimate large scale, volume-averaged permeability and identify localized zones of relatively high permeability and fluid flow (Figure 8). Equilibrated static temperature (T) profiles in geothermal systems record the relative role of conductive and advective heat transport. Under near steady-state conditions these profiles can reveal the long-term average permeability (k) along the T profile to an order of magnitude by solving for the advective component. Fluid inclusion homogenization temperatures that reflect the modern temperature profile are consistent with this assumption (Figure 8; Moore et al., 2004). Well 58A-10 in the undisturbed margin of the CGF offers the opportunity to quantify vertical variations in k that provide a critical insight into the life cycle of geothermal systems. This well has four zones of distinctly different T gradient (Figure 8; zones discussed further below): Zone 1, a near-surface boiling zone characterized by steep temperature gradients that vary markedly between well logs at different times; Zone 2, a shallow conductive zone from 400 to 1100 m depth with gradients ~100°C/km; Zone 3, a near-isothermal convective zone from 1100 to 2900 m; and Zone 4, a basal conductive zone >2900 m with gradients ~100°C/km. In the following analysis, we analyze temperature profiles from Zones 2 and 3 to infer permeability variations using simple analytical steady-state solutions for 1-D heat transport and convective instability. This analysis utilizes the Boussinesq approximation assuming constant fluid properties and porous media flow.

5.3.1 Zone 2: Conductive

Intervals of high temperature gradient imply a predominance of conductive heat transfer and limited permeability (Zone 2 in Figure 8). For this analysis we assume that variations in temperature gradient in well 58A-10 primarily reflect variations in the relative contributions of conductive heat flux, which depends on the thermal conductivity of the rock, and advective heat transport, which primarily depends on the rate and direction of fluid flux (see discussion in Ingebritsen and Sanford, 1998). For steady laminar vertical flow within a vertical interval of length (thickness), L, with constant temperature lower, T_L, and upper, T_U, boundaries, analogous to a laterally semi-infinite low permeability layer between two high permeability layers, the temperature, T_z, at intermediate depth, z, between the upper and lower boundaries is given by (Bredehoeft and Papadopolous, 1965):

$$(T_z - T_U) / (T_L - T_U) = f(\beta, z/L) \quad (5.1)$$

$$f(\beta, z/L) = [\exp(\beta * z/L) - 1] / [\exp(\beta) - 1] \quad (5.2)$$

$$\beta = c_w \rho_w q_w L / K_m \quad (5.3)$$

where β is a dimensionless parameter expressing the relative contributions of conductive and convective heat transport (negative for fluid up-flow and positive for down-flow), c_w is the isochoric heat capacity of water [J/°K], ρ_w is the density of water [kg/m³] , q_w is the average volumetric flow rate per unit area of water [m/s], K_m is the bulk thermal conductivity of saturated rock [W/(m·°K)].

Table 1: Properties of rocks and fluid in thermal model. Subscripts U and L denote upper and lower boundaries of layer and M denotes its midpoint.

Parameter		Zone 2	Zone 3
Depth [m TVD below GL]			
	z_U	460	1306
	z_M	751	2164
	z_L	1042	3022
Temperature [°K]			
	T_U	353	431
	T_M	383	457
	T_L	765	484
Physical Properties			
Water Density ρ_w [kg/m³]		955	912
Fluid pressure P_f [MPa]		7.00	19.8
Isochoric Heat Capacity of Water c_w [J/°K]		3.71	3.43
Bulk Rock Thermal Conductivity K_m [W/(m·°K)]		3.3	3.3

To estimate *in situ* fluid properties, we assumed that the undisturbed (*i.e.*, pre-production) formation fluid pressure (P_f) was in hydrostatic equilibrium with a water table at the surface. This is consistent with slight positive wellhead pressures recorded prior to significant production in the East Flank, such as in well 64-16 (Paul Spielman, pers. comm., 2003; Joe Moore, pers. comm., 2004). To take account of the high geothermal gradients, the variation of fluid pressure (Figure 6) and other fluid properties with depth was determined by integrating experimentally derived pure water density as a function of pressure and temperature as appropriate to ambient geothermal conditions, and including a small correction for total dissolved solids (Keenan *et al.*, 1978). Representative fluid properties for use in this analysis (assumed constant) were then taken at the mid-point of the modeled depth interval (Table 1; for supporting details see Davatzes and Hickman, 2006a, and Davatzes et al., 2006). We also assumed an average thermal conductivity ~3.3±0.5 W/(m·°K), based on measurements made elsewhere on diorites similar to those encountered in well 58A-10 (Clauser and Huenges, 1995). Here and subsequent sections, we assumed that modern measurements of temperature in well 58A-10 reliably represent pre-production thermal conditions, which is reasonable given the limited injection of cold fluid into the nearby East Flank and lack of hydrologic communication between Coso Wash and producing portions of the CGF (Mike Adams, pers. comm., 2003) and consistency with fluid inclusion homogenizatin temperatures (Figure 8a).

We used equations 5.1 through 5.3 to produce a synthetic temperature profile as a function of the fluid flux (Figure 9a), wherein dimensionless temperature (Equation 5.1) is plotted versus dimensionless depth, $(z - z_u)/(z_L - z_u)$. The solution reveals that the volume averaged advective flow rate, q_w, is $<10^{-10.4}$ m/sec. It should be emphasized that lower flow rates cannot be distinguished in this approach and are also possible. Assuming vertical advection is driven by buoyancy, Darcy's Law provides a relation between the Darcy velocity, the viscosity of water, μ_w [Pa.s], buoyancy per unit volume, P_B [Pa], and permeability, k [m²] as:

$$P_B = \rho_U \alpha_w (T_L - T_U) g = (\rho_L - \rho_U) g \quad (5.4)$$

$$k = -(q_w \mu w) / [P_B] \quad (5.5)$$

where ρ_w is the density of water at temperature T_U, α_w is the volume coefficient of linear thermal expansion [1/°K], *g* is

the acceleration due to gravity [m/s^2], and μ_w is the viscosity of water [Pa·s]. In this approximation we assume that the pressure gradient approximates the hydrostatic gradient at T_u. In this and subsequent calculations, buoyancy force for a unit volume was determined from the density difference at the upper and lower boundaries of the zone assuming density as a linear function of temperature, as given in equation 5.4 (Norton and Cathles, 1979; Ingebritsen and Sanford, 1998; Turcotte and Schubert, 2002). From equation 5.5, the rate of flow requires a permeability of $<10^{-16.5}$ m^2 (Figure 9b and Figure 8d).

This analysis indicates that conductive heat transport can account for all of the heat transport within the cap rock (Zone 2). Although extremely simple in that this analysis neglects lateral heat transfer, heat from chemical reactions or radioactive decay, or time-varying fluid velocity, and assumes a constant volume averaged permeability, these effects should only reduce the fluid flux necessary to match the temperature profile, making this a good upper bound on permeability in this depth interval.
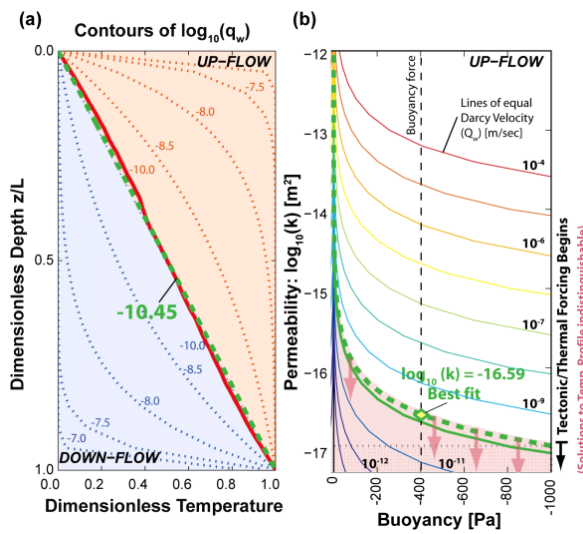

Figure 9: Solution for 1-D up-flow or down-flow of a low permeability unit between an infinite fluid source and sink. (a) Doted lines: temperature profiles associated with indicated log$_{10}$ volumetric flow rates, q$_w$, where down-flow and up-flow contours are concave up and concave down, respectively. Solid line: measured temperature profile from Zone 2 in well 58A-10. Dotted green line: best-fit log$_{10}$ volumetric flow rate. (b) Darcy flow velocity depends on a combination of buoyancy driving flow and permeability resisting flow. An estimated buoyancy force of 400 Pa suggests permeability $<10^{-16.5}$ m^2 (see text).

5.3.2 Zone 3: Convective Zone

Regions of near-isothermal temperatures imply significant convective heat transfer and high permeability within the geothermal reservoir underlying the cap rock (Zone 3 in Figure 8). If convection is driven by buoyancy force, then the permeability required to initiate a convection cell of a given height, L [m], can be determined from the critical Rayleigh Number, Ra$_{crit}$, (Turcotte and Schubert, 2002) as:

$$Ra = \frac{P_B \rho_w c_w kL}{\mu_w K_m} = Ra_{crit} = 4\pi \qquad (5.6)$$

$$\frac{dT_c}{dz} = \frac{4\pi^2 \mu_w K_m}{P_B \rho_w c_w} \frac{1}{kL^2} \qquad (5.7)$$

where the variables are as in equations 5.1 through 5.5, and dT_c/dz is the critical temperature gradient [°K/m]. Ra$_{crit}$, is related to the dT_c/dz in equation 5.7 by P_B's dependence on temperature gradient (equation 5.4). In this analysis as before, we assume that fluid properties are constant and can be approximated by values at the center of Zone 3 derived from the equation of state for water (Table 1). For up-flow driven by buoyancy due to heating from below, this analysis suggests that the minimum average permeability required for the near isothermal temperature gradients in the convecting interval of well 58A-10 is $10^{-13.0}$ to $10^{-14.6}$ m^2 (Figure 10). Even higher minimum permeabilities are required over shorter intervals of the well in Zone 3, where lower temperature gradients are observed (yellow diamonds in Figure 10a and yellow dots in Figure 8d).
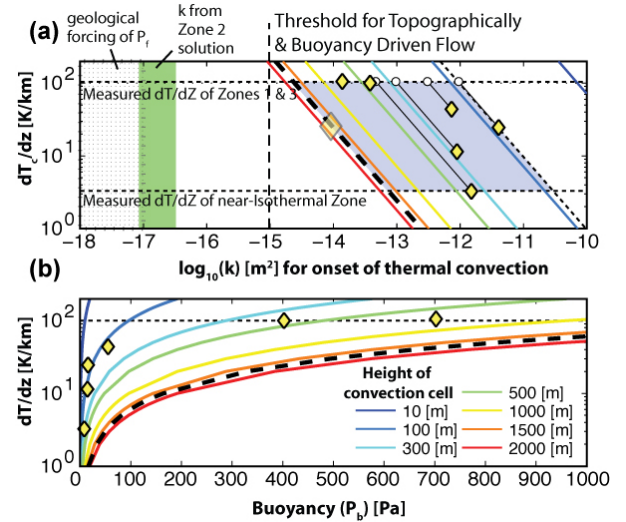

Figure 10: Required temperature gradient for the onset of buoyancy-driven convective flow consistent with observed temperatures (Figure 8a,b). (a) Minimum permeability for convective flow determined using the critical Rayleigh Number and temperature gradients across discrete intervals of Zone 3 (Figure 8). Higher temperature gradients correspond to greater buoyancy and a reduced minimum permeability. Diamonds represent the calculated permeabilities for a given combination of temperature gradient and inferred convection cell height (see legend in 10b). Larger diamond represents the average temperature gradient across Zone 3. Horizontal dashed lines reflect the range of temperature gradient observed in well 58A-10, while the inclined dashed lines coincide with the range of permeabilities of different temperature gradient sub-zones (Figure 8), thus Blue rhomb outlines the ranges of values possible within the near isothermal zone. Stippled region to left indicates permeability at which tectonic strain rates are sufficient to produce overpressure (Ingebritsen and Sanford, 1998). (b) Magnitude of buoyancy as a function of temperature gradient and convection cell height (from Equations 5.5, and 5.7).

Alternatively, if heat flux is 1-D (vertical), then the advective heat flux, fluid flux and permeability through Zone 3 can be estimated by balancing the heat flux through Zones 2 and 4. Zones 2 and 4 share nearly identical mineralogy and temperature gradient suggesting a similar dominance of conductive over advective heat flux, as discussed above for Zone 2. The total heat flux across Zone

3 must then be the sum of the advective and conductive parts (following the same assumptions as above) and match the input from Zone 4 and output into Zone 2. In Zones 2 and 4, treating these as purely conductive, the total heat flux is $K_m(T_L-T_U)/L$ = 2.33 mW/m^2, where $K_m^{(zone\ 2)} \approx K_m^{(zone\ 3)}$ = 3.3 W/(m*K). Then in Zone 3, the advective heat flux, $q_h^{(advective)}$, is given by the difference of the total heat flux, $q_h^{(total)}$, and the conductive heat flux, $q_h^{(conductive)}$, and thus q_w = $q_h^{(advective)}$ / ($c_w\ \rho_w\ T_{mean}$) = 1.49 x 10^{-6} m/sec. If driven by buoyancy force as before, then the permeability in Zone 3 required to match the observed temperature gradient is k = q_w (dP_b/dz) ≈ 10$^{-13.0}$ to 10$^{-11.5}$ m^2. This estimate agrees fairly well with that obtained from our convective instability analysis (Figure 10).

These approaches both assume a 1-D model of fluid upwelling and a constant volume-averaged Darcy velocity. In reality, fluid velocities, and thus permeability or driving pressure, must increase as the fracture spacing increases, *i.e.*, as the number of fractures hosting fluid flow decreases. Fluid flow concentrated into such discrete zones is consistent with anomalies in temperature gradients that occur over wavelengths of less than a few tens of meters (Davatzes and Hickman, in press). Thus, the average temperature gradient in Zone 3 requires $k>10^{-14}$ m^2 (large yellow diamond in Figure 10a), with much higher local excursions in permeability (Figure 8d). Thus, there is a $>10^3$ k difference between Zones 2 and 3 despite similar host rocks and fracture density (see Davatzes and Hickman, in press).

6. CONCEPTUAL MODEL FOR THE EVOLUTION OF PERMEABILITY IN THE COSO GEOTHERMAL SYSTEM

The distribution of active fumaroles and steaming ground at the surface (Figure 1c) indicate that fluid flow is primarily associated with active fault segments trending NNE and at intersections between fault segments. However, not all of the faults (or fault segments) with high slip tendency mapped in the CGF appear to be permeable. For example, as discussed above, the temperature profiles (Figures 8 and 11) and geologic well log from well 58A-10 suggest that the conductive zone (Zone 2) is associated with abundant clay mineralization, in contrast to the convecting zone (Zone 3) which is associated with calcite precipitation and little alteration. Thus, even though fractures that are well oriented and stressed for frictional failure exist in both of these zones (Davatzes and Hickman, 2009), only those in Zone 3 have significant permeability.

Furthermore, the mineralogy and texture of the different fault zones identified at Coso (Figures 2 through 4, and 11) indicate the role of different deformation mechanisms and structural/geochemical history. For example, faults healed by the precipitation of calcite and related minerals continue to undergo brittle dilation when reactivated and thus regenerate permeability. In contrast, the introduction of chlorite and other sheet silicates such as smectite appear to promote ductility and thereby minimize dilatancy of the fault rock during shear. These differences can account for the greater than three order of magnitude disparity in vertical permeability between Zones 2 and 3 (Figure 8d). In the following sections we discuss the relationship of the deformation mechanisms that control fluid flow to the deformation environments defined by the shallow ground water system, clay-rich caprock, reservoir interval, and deeper conductive zone that define the Coso Geothermal System. This reservoir model is illustrated in Figure 11 and indexed to the four zones shown in Figure 8.
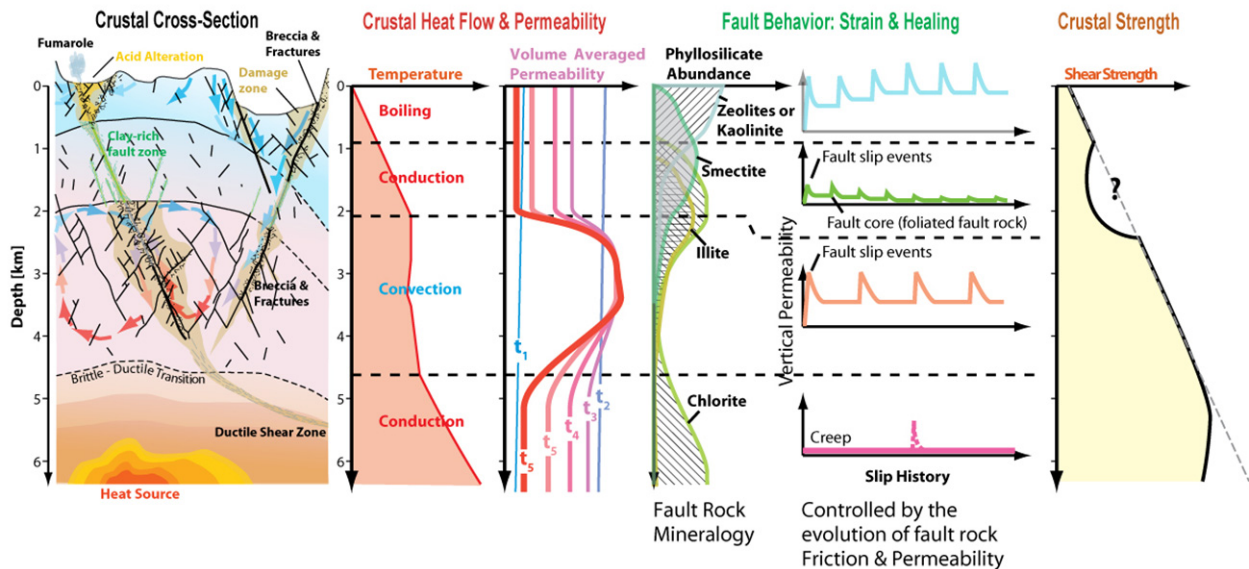

Figure 11: Schematic diagram showing how cycles of deformation and chemical reactions along faults can control the evolution of fault zone strength, frictional behavior, and hydrologic properties. a) Idealized cross-section showing fluid circulation along faults and fractures, b) related temperature gradient, c) evolution of permeability with time as the geothermal system evolves (starting at t1, reaching final hydrological stratification at t5), d) distribution of phyllosilicate mineral phases controlling fault slip, hydrologic evolution and long-term (average) crustal strength, e) schematic showing periodic regeneration of vertical permeability in each zone through fault slip and dilation i, and e) conceptual model for variation in long-term crustal strength, including possible shear stress reduction in smectite-rich conductive cap rock.

Zone 1. Shallow groundwater flow: In the shallowest zone, groundwater flow circulates through a network of diffusely distributed fractures associated with active faulting and dilatant failure facilitated by low confining stress . Rising geothermal fluids or boiling in areas of high heat flow and slow recharge exsolve gases that can mix with shallow groundwater, potentially lowering the pH and promoting mineral dissolution (Facca and Tonani, 1967). Dissolution of major rock-forming minerals such as feldspar, plagioclase, hornblende, pyroxene and biotite should initially increase fault zone permeability (e.g., Figure 3). This overall gradual increase in permeability will be augmented by sudden permeability increases induced by dilatancy accompanying episodic fault slip (spikes in blue line in Figure 11e).

Zone 2. Caprock: The caprock is characterized by conductive heat flow and minimal circulation of fluid. Initial fault formation and slip is the result of brittle-dilatant failure. However, continued slip and fluid flow leads to the formation of smectite phases and chlorite along faults, primarily along slip surfaces where reaction is facilitated by cataclasis, grain size reduction and formation of fresh surfaces that facilitate dissolution and act as nucleation sites for precipitation (e.g., Figures 4 and 5). These clay minerals deform ductily, thereby sealing fractures and inhibiting further dilation during slip. This ductile flow is accommodated by grain rotation, folding and basal shear. Pores in clay-rich gouge are small (< 0.01 μm) and poorly connected (Figure 5). In the examples examined thus far, pore dimensions correspond directly with the grain size of the clay gouge and the thickness of gouge layers separated by slip surfaces. Fault rocks enriched in neoformed clays minimize dilation during slip and can reduce k to lower than 10^{-19} m^2 (see section 3.2, Crawford et al., 2001; Tembe et al., in press). The key aspects of clay gouge development are the formation of multiple slip surfaces and the precipitation of new clay minerals in the open pores adjacent to slip surfaces and gouge layers that are subsequently sheared and compacted.

Alteration is greatest in the fault core and decreases into the host rock (Figure 4), where local cycles of cataclasis and brecciation followed by healing are evident. As a result, much of the damage outside the fault core in unaltered rock remains dilatant. Consequently, fault-parallel permeability increases as cross-fault permeability decreases. The net result is the progressive development of faults with low cross-fault permeability and enhanced fault-parallel permeability. Although permeability might increase in the fault damage zones, the intersection of non-parallel (e.g., conjugate) fault cores truncates the damage zone, leading to a caprock with low overall permeability consistent with the vertically stratified permeability indicated in Figure 8d. Since the stability of clays is restricted to relatively low temperature <150-200°C (Meneur, 2005), clay-rich faults are confined to shallow depths, consistent with findings by (More et al., 2004; Kovac et al., 2005). Thus, a fault core enriched in clays at shallow depths becomes a persistent barrier to cross-fault flow that effectively reduces vertical k. Over the lifetime of the geothermal system, continued alteration should further isolate and reduce the size of zones of dilatant failure that generate fracture permeability.

The vertical permeability seal provided by this "clay-rich cap" could be breached by the development of (1) new fault networks or (2) localized dilation related to large-scale interactions between non-planar faults. New fault networks form when there is a sudden change in tectonic stress that is unfavorable for reactivation of an established fault network. Because alteration is primarily localized along the older fault networks, new faults will principally propagate through nearly unaltered rock that favors brittle failure. Owing to the low frictional strength of most clays (Lockner and Beeler, 2002), large rotations of the principal stresses would be required to create new faults in a clay-rich cap, suggesting that breaching of the cap rock by new fault networks will be more difficult. Also, mechanical interaction of fault segments at extensional steps or intersections can locally produce large rotations and decreased mean stress that promote dilatant failure (Davatzes *et al.*, 2005). This mechanism could produce a pathway for fluids to migrate from reservoir depths to the surface along parts of faults—essentially breaching the cap rock, resulting in fumaroles or other surface manifestations of hydrothermal activity.

For example, in the highly permeable geothermal reservoir of the East Flank the height of major basin-bounding normal faults are approximately 1 to 2 times the fault trace length, whereas the spacing between these major faults is 1 to 0.2 times the fault trace length (see Figure 1b). This geometry promotes mechanical interaction and the transfer of stress from one fault to another, leading to localized stress heterogeneities and deformation between interacting faults. Along-strike relays between these obliquely slipping normal fault segments thus can create vertically extensive fault dilatation leading to fumaroles or other surface manifestations of deeper hydrothermal activity (e.g., Davatzes et al., 2005; Eichhubl et al., 2009).

Zone 3. Reservoir zone: The reservoir zone is dominated by brittle fracture, brecciation, and cataclasis. Healing primarily occurs by the precipitation of calcite or silica (potentially promoted by convection). These minerals retain dilatant behavior during slip that regenerates k as revealed by crack-seal textures in the core (Figure 2) and consistent with the high frictional strength and brittle behavior of the granitic host rocks (see Lockner and Beeler, 2002). In general, the near absence of clays and other phyllosilicates in the reservoir zone prevents the formation of a persistently low-permeability fault core. Thus, across-fault as well as along-fault permeability will be regenerated by periodic fault slip (Figure 11e). In addition, splay fractures emanating off the main slip surfaces should promote connectivity with fractures in the surrounding damage zone leading to the maintenance of vertically extensive permeable conduits for fluid flow.

In detail, reduced grain size in the fault core due to cataclasis increases the area of fresh mineral surfaces and the rate of chemical reactions and precipitation on those surfaces. This suggests that the core of reservoir faults will heal faster than the damage zone during the inter-seismic period and thus produce transient across-fault barriers and low-permeability seals (Byerlee, 1993). Consequently, convection can be temporarily confined within isolated compartments resulting in small steps in temperature gradient (Figure 8b), even though these seals may be periodically ruptured. In this manner, permeability within the main reservoir remains generally high, supporting vigorous convection and yielding isothermal T profiles, as discussed above.

Zone 4. Crystal-plastic deformation below the brittle-ductile transition: The cause of the low permeability in the basal zone is less well defined, although borehole televiewer logs reveal lower fracture density in this zone (Davatzes and Hickman, 2009). It is likely that higher normal stresses and temperatures at these depths act to keep permeability low in

this zone through a combination of asperity destruction by brittle crushing, crystal-plastic deformation, and dissolution and healing of fractures at higher rates than in shallower intervals. Thus, permeability should remain low in this zone, inhibiting advective heat transport.

As temperature increases with depth and proximity to the heat source, crystal plastic deformation becomes the dominant deformation mechanism. Large earthquakes can locally extend the depth of micro-seismicity (as indicated by the jagged top of the brittle-ductile transition in Figure 1b) by locally increasing the strain rate. However, since crack closure following these periodic deep earthquake should be quiet rapid, the permeability of fault and country rock in this zone overall is expected to be quite low.

CONCLUSIONS

Earlier observations suggested that the geometry of active faults in relation to the local state of stress provides one driving mechanism to develop and maintain regions of focused fluid flow in the CGF (Sheridan et al., 2003; Sheridan and Hickman, 2004). However, our observations indicate that fault rock mineralogy and texture provide a further control on the formation and maintenance of fluid flow in the geothermal field. The evolution of this mineralogy and its impact on the evolution of geothermal systems and fault mechanics is a focus of ongoing research.

The feedback between fracture slip driven by stress, the generation of permeability, fluid flow and alteration suggests that fracture permeability will evolve concurrently with the geothermal system. Initial fracture development in unaltered crystalline rocks will enhance permeability and allow the circulation of fluids, the transfer of heat, and initiate chemical alteration. Chemical alteration will eventually lead to the breakdown of rock forming minerals and alteration to clays within appropriate temperature and pressure conditions. The presence of clay in the cap rock mitigates the ability of fracture slip to generate permeability, forming persistent cross-fault fluid barriers and consequently isolating the deeper geothermal reservoir from the surface. In contrast, in reservoir rocks permeability is maintained in fracture systems of calcite- or silica-dominated fracture sealing through dilatancy accompanying episodic slip, despite exposure to the same stress state and deformation conditions as in the cap rock. The implication for Coso is that chemical alteration of otherwise low-porosity crystalline rocks appears to determine the distribution and temporal evolution of permeability in the actively deforming fracture network at small to moderate scales as well as along major, reservoir-penetrating fault zones.

REFERENCES

Adams, M.C., J.N. Moore, S. Bjornstad, and D.I. Norman (2000), Geologic history of the Coso geothermal field. *Proceedings World Geothermal Congress 2000, Kyushu – Tohoku, Japan, May 28 – June 10, 2000*. p. 2463-2469.

Antonellini, M.A. and A. Aydin (1994), Microstructure of deformation bands in porous sandstone at Arches National Park, Utah. *Journal of Structural Geology*, v. 16, p. 941-959.

Aydin, A., Johnson, A.M. (1978), Development of faults as zones of deformation bands and as slip surfaces in sandstone. *Pure and Applied Geophysics*, v. 116, p. 931 – 942.

Barton, C. A., S. Hickman, R. Morin, M.D. Zoback, and D. Benoit, (1998), Reservoir-scale fracture permeability in the Dixie Valley, Nevada, Geothermal Field, *Proceedings 23rd Workshop on Geothermal Reservoir Engineering*, Stanford University, p. 299–306.

Bishop, B.P. and D.K. Bird (1987), Variation in sericite compositions from fracture zones within the Coso Hot Springs geothermal system. *Geochimica et Cosmochimica Acta*, v. 15, p. 1245-1256.

Boitnott, G.N. (2002), Core analysis for the development and constraint of physical models of geothermal reservoirs. *Geothermal Research Council Transactions*, v. 26, p. 387-392.

Bredehoeft, J.D. (1965), and Papadopolous, I. S. Rates of vertical groundwater movement estimated from the Earth's thermal profile. Water Resources Research, v. 1, p. 325-328.

Brown, S.R. (1987), Fluid flow through rock joints: Effects of surface roughness. *Journal Geophysical Research* v. 99, p. 9373-9390.

Byerlee, J. (1978), Friction of rocks. *Pure and Applied Geophys.*, v. 116, p. 615-626.

Byerlee, J.D. (1993), A model for episodic flow of high pressure water in fault zones before earthquakes. *Geology*, v. 21, p. 303-306.

Clauser, C. and E. Huenges (1995), Thermal Conductivity of Rocks and Minerals, *In:* T. Ahrens, ed., AGU Handbook of Physical Constants, American Geophysical Union, New York, p. 105-126.

Crawford, B.R., R.D. Myers, Woronow, A., (2002), D.R. Faulkner, and E.H. Rutter: Porosity-permeability relationships in clay-bearing fault gouge. *SPE/IRSM*, v. 78214, p. 1-13.

Davatzes, N.C. and A. Aydin (2003), The formation of conjugate normal fault systems in folded sandstone by sequential jointing and shearing, Waterpocket monocline, Utah. *Journal of Geophysical Research*, v. 108(B10), p. 2478-2493.

Davatzes, N.C. and S. Hickman (2005a), Comparison of acoustic and electrical image logs from the Coso geothermal field, CA. Proceedings, *30th Workshop on Geothermal Reservoir Engineering*, Stanford University, January 31- February 2, 2005. SGP-TR-176, p. 1-11.

Davatzes, N.C. and S. Hickman (2005b), Controls on Fault-Hosted Fluid Flow: Preliminary Results from the Coso geothermal field, CA, *Geothermal Resources Council Transactions*, v. 29, p. 343-348.

Davatzes, N., and S. Hickman: Stress, fracture and fluid flow analysis using acoustic and electrical image logs in fractured granites of the Coso Geothermal Field, Nevada, in *Dipmeter and Borehole Image Log Technology*, M. Pöppelreiter et al. (eds), AAPG Memoir, Chapter 24 (in press).

Davatzes, N.C., P. Eichhubl, and A. Aydin (2005), Structural evolution of fault zones in sandstone by multiple deformation mechanisms; Moab Fault, southeast Utah. *Geological Society of America Bulletin*, v. 117(1-2), p. 135-148.

Davatzes, N.C. and S. Hickman (2006a), Stress and faulting in the Coso Geothermal Field: Update and recent results from the East Flank and Coso Wash:

Proceedings, 31st Workshop on Geothermal Reservoir Engineering, Stanford University, Stanford California, January 30-February 1, 2006, SGP-TR-179, v. 31, 12 p.

Davatzes, N.C. and S.H. Hickman (2006b), Section 3.1 Mechanical, Mineralogical, and Petrophysical Analysis of Fracture Permeability: *in* Rose, P., *et al*, Progress Report for Year Ending December 31, 2005: Creation of an Enhanced Geothermal System through Hydraulic and Thermal Stimulation: Report to DOE, grant # DE-FC07-01ID14186, 239 p., p. 135-164.

Davatzes, N.C., Hickman, S.H., Sheridan, J. (2006), Section 2.1 Fracture and Stress Analysis: *in* Rose, P., *et al.*, Progress Report for Year Ending December 31, 2005: Creation of an Enhanced Geothermal System through Hydraulic and Thermal Stimulation: Report to DOE, grant # DE-FC07-01ID14186, 239 p. 11-37.

Davatzes, N.C. and Hickman, H. (in press), Stress, fracture, and fluid-flow analysis using acoustic and electrical image logs in hot fractured granites of the Coso geothermal field, California, in M. Poppelreiter, ed., Dip-meter and borehole image log technology: *American Association of Petrolium Geologists Memoir,* v. 92, p. 1–35.

Duffield, W.A., C.R. Bacon and G.B. Dalrymple (1980), Late Cenozoic volcanism, geochronology, and structure of the Coso Range, Inyo County, California. *Journal of Geophysical Research*, v. 85(B5), p. 2381-2404.

Eichhubl, P, N.C. Davatzes, S.P. Becker (2009), Structural and diagenetic control of fluid migration and cementation along the Moab Fault, Utah. *American Association of Petroleum Engineers*, v. 93(5), p. 653-681.

Facca, G. and F. Tonani (1967), The self-sealing geothermal field. *Bulletin of* Volcanology, v. 30, p. 271-273.

Feng, Q. and J.M. Lees (1998), Microseismicity, stress, and fracture in the Coso geothermal field, California. In: *Tectonophysics*, v. 289, p. 221-238.

Geomechanics International (2003), Fracture permeability and *in situ* stress in the Eastern Extension of the Coso Geothermal Reservoir: Kinematic and dynamic studies of the Coso Geothermal and surrounding area. *Report prepared for Geothermal Program Office, Contract Number N68936-01-R-0095*, 75 p.

Hickman, S., M.D. Zoback and R. Benoit (1998), Tectonic controls on reservoir permeability in the Dixie Valley, Nevada, geothermal field, *Proceedings 23rd Workshop on Geothermal Reservoir Engineering*, Stanford Univ. p. 291–298.

Hulen, J.B.: Geology and alteration of the Coso geothermal area, Inyo County, California. U. S. Department of Energy: Geothermal Energy. (1978).

Ingebritsen, S.E., W.E. Sanford, and C.E. Neuzil (2006), Groundwater in Geologicl Processes; 2nd Edition: Cambridge University Press, 536 p.

Jaeger, J.C. and N.G.W. Cook (1979), Fundamentals of Rock Mechanics (Third Edition). New York, Chapman and Hall, 539 p.

Keenan J.H., F.G. Keys, P.G. Hill, and J.G. Moore (1978), Steam Tables: Thermodynamic Properties of Water Including Vapor, Liquid, and Solid Phases, John Wiley & Sons, New York, 156 pp.

Kovak, K.M., J.N. Moore, and S.J. Lutz (2005), Geologic Framework of the East Flank, Coso Geothermal Field: Implications for EGS Development. *28th Workshop on Geothermal Reservoir Engineering*, Stanford University, Stanford, California, January 31-Februrary 2, SGP-TR-176, 7 p.

Lockner, D.A. and N.M. Beeler (2002), Rock failure and earthquakes. International Handbook of Earthquake and Engineering seismology, v. 81A, p. 505-537.

Lutz, S.J., J.N. Moore, and J.F. Copp (1996), Integrated mineralogical and fluid inclusion study of the Coso geothermal system, California. *Proceedings 21st Workshop on Geothermal Reservoir Engineering, Stanford, CA, Jan 22-Jan 24*, p. 187-194.

Manley, C.R. and C.R. Bacon (2000), Rhyolite thermobarometry and the shallowing of the magma reservoir, Coso Volcanic Field, California. *Journal of Petrology* v. 41, p. 149-174.

Meneur, A. (2005), *Clays*, New York, Springer, 472.

McCluskey, S.C., Bjornstad, B.H. Hager, R.W. King, B.J. Meade, M.M. Miller, F.C. Monastero, and B.J. Souter (2001), Present day kinematics of the Eastern California Shear Zone from a geodetically constrained block model. *Geophysical Research Letters*, v. 28(17), p. 3369-3372.

Monastero, F.C., A.M. Katzenstein, S.J. Miller, J.R. Unruh, M.C. Adams and K. Richards-Dinger (2005), The Coso geothermal field: A nascent metamorphic core complex. *Geological Society of America Bulletin*, v. 177(11/12), p. 1534-1553.

Moore, J., D. Norman and M. Adams (2004), Thermal and chemical history of the Eastern Coso geothermal field. Report to the Navy Geothermal Program Office, Report N68936-01-0095, 71 p.

Morrow, C.A. and D.A. Lockner (2006), Physical properties of two core samples from well 34-9RD2 at the Coso geothermal field: U.S. Geological Survey, Reston, VA, United States. Open-file Report 2006-1230, 32 p.

Norton, D. and L.M. Cathles (1979), Thermal aspects of ore deposits, in: Barnes, H.L., ed., *Geochemistry of Hydrothermal Ore Deposits*, New York, John Wiley and Sons. p. 611-631.

Peska, P. and M.D. Zoback (1995), Observations of borehole breakouts and tensile wall fractures in deviated boreholes: A technique to constrain in situ stress and rock strength. *Journal of Geophysical Research*, v. 100, p. 12791-12811.

Rodgers, K.A., P.R.L. Browne, T.F., Buddle, K.L. Cook, R.A. Greatrex, W.A. Hampton, N.R. Herdianita, .R. Holland, B.Y. Lynne, R. Martin, Z. Newton, D. Pastars, K.L. Sannazarro, and C.I.A. Teece (2004), Silica phases in sinters and residues from geothermal fields of New Zealand, Earth-Science Reviews, v. 66, p. 1-61.

Roquemore, G. (1981), Active Faults and Associated Tectonic Stress in the Coso Range, California. Naval Weapons Center, China Lake, California 93555, China Lake, CA, 101 p.

Roquemore, G. (1984), Structure, tectonics, and stress field of the Coso Range, Inyo County, California. *Journal of Geophysical Research*, v. 85(B5), p. 2434-2440.

Sheridan, J., K.M. Kovac, P.E. Rose, C.A. Barton, J. McCulloch, B. Berard, J.N. Moore, S. Petty and P.

Spielman (2003), In situ stress, fracture and fluid flow analysis-East Flank of the Coso geothermal field. *28ᵗʰ Workshop on Geothermal Reservoir Engineering*, Stanford University, Stanford, California, January 27-29, SGP-TR-173, 16 p.

Sheridan, J. and S. Hickman (2004), In situ stress, fracture and fluid flow analyses in well 38C-9: An enhanced geothermal system in the Coso geothermal field, *29ᵗʰ Workshop on Geothermal Reservoir Engineering*, Stanford University, Stanford, California, January 26-28, SGP-TR-175, 8 pp.

Tembe, S., D. A. Lockner, and T.-f. Wong (in press), Effect of clay content and mineralogy on frictional sliding behavior of simulated gouges: Binary and ternary mixtures of quartz, illite and montmorillonite, Journal of Geophysical Research.

TerraTek (2004), Physical and mechanical properties characterization of two granitic rocks, Coso EGS Project, TerraTek Inc., *Technical Report TR04-400872*, Salt Lake City, UT, 71 p.

Turcotte D.L. and G. Schubert (2002), Geodynamics; Second Edition, John Wiley & Sons, New York, 456 p.

Unruh, J.R., E. Hauksson, F.C. Monastero, R.J. Twiss, and J.C. Lewis: Seismotectonics of the Coso Range—Indian Wells Valley region, California: Transtensional deformation along the southeastern margin of the Sierran microplate, in: Glazner, A.F., Walker, J.D., and Bartley, J.M., (eds), Geological evolution of the Mojave Desert and Southwestern Basin and Range: Boulder, CO, *GSA Mem.*, **195**, (2002), 227-294.

Unruh, J. R. and E. Hauksson (2003), Seismotectonics of an Evolving Intra-Continental Plate Boundary, East-Central California. Geothermal Program Office Technical Symposium 8, University of California, Davis, CA.

Unruh, J.R., and A.R. Streig (2004), Mapping and characterization of neotectonic structures in a releasing stepover, northern Coso Range, eastern California: Final technical report submitted to the U.S. Navy Geothermal Program Office, China Lake Naval Air Warfare Center, Contract N68936-02-C-0208, 46 p.

Whitmarsh, R.S. (1998), Geologic map of the Coso Range: *Geological Society of America on-line map, doi: 10.1130/1998-whitmarsh-coso*.

Whitmarsh, R.C. (1998), Structural development of the Coso Range and adjacent areas of eastern California [Ph.D. thesis]: Lawrence, Kansas, University of Kansas.

Wicks, C.W., W. Thatcher, F.C. Monastero, and M.A. Hasting (2001), Steady-state deformation of the Coso Range, East-Central California, inferred from satellite radar interferometry, *Journal of Geophysical Research*, v. 106(B7), p. 13769-13780.